

1 Generative AI for image reconstruction in Intensity Interferometry: a first attempt

2 KM NITU RAI,^{1,2} YURI VAN DER BURG,³ SOUMEN BASAK,¹ PRASENJIT SAHA,³ AND SUBRATA SARANGI^{4,5}

3 *School of Physics, Indian Institute of Science Education and Research Thiruvananthapuram, Maruthamala PO, Vithura,*
4 *Thiruvananthapuram 695551, Kerala, India.*

5 *Aryabhatta Research Institute of Observational Sciences, Manora Peak, Nainital 263129, India.*

6 *Physik-Institut, University of Zurich, Winterthurerstrasse 190, 8057 Zurich, Switzerland.*

7 *School of Applied Sciences, Centurion University of Technology and Management, Odisha-752050, India.*

8 *Visiting Associate, Inter-University Centre for Astronomy and Astrophysics, Post Bag 4, Ganeshkhind, Pune 411 007, Maharashtra,*
9 *India.*

ABSTRACT

In the last few years Intensity Interferometry (II) has made significant strides in achieving high-precision resolution of stellar objects at optical wavelengths. Despite these advancements, phase retrieval remains a major challenge due to the nature of photon correlation. This paper explores the application of a conditional Generative Adversarial Network (cGAN) to tackle the problem of image reconstruction in II. This method successfully reconstructs the shape, size, and brightness distribution of simulated, fast-rotating stars based on a sparsely sampled spatial power spectrum obtained from a hypothetical ground-based II facility composed of four Imaging Atmospheric Cherenkov Telescopes (IACTs). Although this particular example could also be addressed using parameter fitting, the results suggest that with larger arrays much more complicated systems could be reconstructed by applying machine-learning techniques to II.

1. INTRODUCTION

Humans instinctively feel a relationship with the stars. One of the primary scientific projects of humanity is to figure out what the stars are and how do they do what they do. The first obvious step in this project, beyond measuring their global parameters like diameter, mass, orbital and astrometric elements, is to obtain images of the stars with all details of the stellar surfaces. In case of the Sun, this is done routinely by observatories and Sun-observation satellites. But such a routine still remains a challenge even for the α -Centauri system, our nearest stellar neighbour. The objective is to achieve capability of high fidelity image reconstruction of distant stars. Two interferometry based techniques, namely, Michelson Interferometry (MI) or Intensity Interferometry (II) have emerged during the last century to address this objective. A discussion of the development of these two approaches and comparison of their respective merits and challenges can be found in (Rai et al. 2025). The work reported here presents the results of a first effort at applying a Conditional Generative Adversarial (neural) Network (cGAN) to image reconstruction of a fast rotator using its simulated II observations.

The foundational basis of II stems from the pioneering experiments and theoretical investigations carried out initially by Hanbury Brown and Twiss (HBT) (Han-

bury Brown & Twiss 1956; Hanbury Brown et al. 1957, 1958) and, later, by (Glauber 1963) and others. The correlation between photons (called the , widely referred to as the “HBT effect”) measured by a pair of photon detectors in two partially coherent beams of light was reported in 1956 Hanbury Brown & Twiss (1956). Rai et al. (2025) present a recent variant of this experiment, carried out with pseudo-thermal light. The HBT Effect and the related theoretical investigations laid the foundation for the modern field of Quantum Optics.

Hanbury Brown and his collaborators led the creation and installation of the historic II facility at Narrabri, Australia, and reported the measurement of angular diameters of 32 stars and a few multiple star-systems (Hanbury Brown et al. 1974). Soon after this work, however, II observations of stars was stalled for over four decades due to the limits of the then available photon detectors and data processing equipment. With gradual mitigation of such issues, proposals to utilize Imaging Atmospheric Cherenkov Telescope (IACT) facilities for conducting II observations of stars have emerged(Le Bohec 2006; Nuñez et al. 2010, 2012a; Dravins et al. 2013) as a secondary science application of these facilities during moonlit nights. SII observations at VERITAS, MAGIC, and H.E.S.S. are now being reported (e.g., Acharyya et al. 2024; Abe et al. 2024; Vogel et al. 2025).

This approach has the potential to enhance the scientific output of existing IACT facilities, and especially of the upcoming Cherenkov Telescope Array Observatory (CTAO). Simulations (Rai et al. 2021, 2022, e.g.,) have shown that recent advancements in photon detectors could be effective in achieving high-precision measurements of parameters for stellar objects.

The thrust of these efforts has been to measure the average global parameters of stars and star systems. High-fidelity imagery, however, would transcend the measurement of global and average stellar parameters, such as angular diameters, binary separations, and orbital characteristics, which offer only an integrated view of the star or star system as a whole. Such imaging capabilities promise direct insights into the dynamic surface phenomena, including limb darkening, convection cells, granulation, star spots, oblateness and gravity darkening in rapid rotators and atmospheric structures, akin to the detailed observations routinely conducted on our own Sun.

As it stands today, studies grappling various issues of image reconstruction are being reported (Haubois et al. 2009; Norris et al. 2021; Liu et al. 2024; Liu et al. 2025). MI-based image reconstruction has made substantial progress in this area with efforts at generating constructed images of stars like Betelgeuse (Haubois et al. 2009) and AZ Cyg (Norris et al. 2021). On the other hand, II-based methods are at a nascent stage. Some recent publications Liu et al. (2024); Liu et al. (2025) have demonstrated, through outdoor experiments, imaging millimeter-scale targets at 1.36 km with a resolution 14 times better than a single telescope’s diffraction limit. A “flexible computational algorithm” reconstructs images from intensity correlations, overcoming atmospheric turbulence and optical imperfections.

We report here, the results of our attempt – the first of its kind – to construct the gravity-darkened sky-image of fast rotating stars consistent with their respective simulated ground-based II-observations using a cGAN neural network architecture. Image reconstruction in gravity-darkened fast-rotating stars has long been examined using various methods in MI (van Belle et al. 2001; Domiciano de Souza et al. 2003, 2005; McAlister et al. 2005; Monnier et al. 2007; Pedretti et al. 2009; Zhao et al. 2009; Martinez et al. 2021). Recently photosphere oblateness of γ -Cassiopeia (Archer et al. 2025) has been measured at the VERITAS observatory using II. These results put our work in context, and our work presented here is a natural next step especially of the work by Archer et al. (2025). We implement a cGAN model (Isola et al. 2017) to reconstruct images of fast-rotating stars using their simulated Intensity Inter-

ferograms and sky-intensity distributions as input data for training, testing, and validation. We consider an array of four Imaging Cherenkov Telescopes (IACTs) whose relative positions approximately mimic those at VERITAS and simulate observations of a set of synthetically generated fast-rotating stars. The image predicted by the trained cGAN shows promising results in reconstructing the stars’ shapes and sizes. The reconstructed brightness distributions are then assessed using moments.

This paper is organized as follows. The next section discusses briefly the past efforts at image reconstruction on II, followed by the section on a discussion of II, focusing on its signal and noise characteristics for fast-rotating stars along the Earth’s rotation. The following section introduces the cGAN formulation and its structure. The fifth section details the parameter selection for training the network for image reconstruction. The sixth section presents the results of the trained network both visually and via image moments. Finally, the paper concludes with a discussion of the overall results.

2. PAST EFFORTS AT IMAGE RECONSTRUCTION RELEVANT TO INTENSITY INTERFEROMETRY

Several approaches have been developed for phase reconstruction in intensity interferometry (II). Gamo (1963) introduced triple-intensity correlation, applied by Goldberger et al. (1963) to microscopic systems and extended by Sato et al. (1978, 1979, 1981) to measure stellar diameters and phases, though limited by low signal-to-noise ratio (SNR). Gerchberg (1972) proposed an iterative phase retrieval method using image and diffraction plane data, sensitive to initial estimates and convergence speed. Fienup (1982) improved this with the Hybrid Input-Output algorithm, enhancing robustness in noisy conditions. Holmes et al. (2010) utilized Cauchy-Riemann relations for 1-D and 2-D image reconstruction, applied to simulated stellar data with Imaging Cherenkov Telescope Arrays (Nuñez et al. 2010, 2012a,b), but faced computational complexity for higher dimensions. Li et al. (2014) introduced a regularized iterative method incorporating priors (e.g., sparsity) to mitigate noise and ill-posedness, though challenged by parameter tuning and initial guess sensitivity. The Transport-of-Intensity Equation (TIE), proposed by Teague (1983), retrieves phase from intensity variations across planes; Zhang et al. (2020) solved TIE as a Poisson equation using a maximum intensity assumption, while Kirisits et al. (2024) combined TIE with the Transport of Phase Equation for improved accuracy across arbitrary apertures and non-uniform illu-

mination, with convergence dependent on initial guesses and boundary conditions.

With non-linearity built into their architecture, artificial neural networks (ANNs) empowered by deep learning methods are promising for exploring the task of reconstructing images of stellar objects from ground-based observations. Convolutional Neural Networks (CNNs), with their specialized architecture for processing two-dimensional datasets, are a natural choice for image processing tasks. In astronomical image reconstruction projects, a common challenge is that the interferometric data are typically undersampled as well as noisy. Therefore, the CNN architectures and deep learning methods employed must be capable of reliably learning both the global context of the training dataset and the local features within it. Among the various CNN architectures, U-Net models (Ronneberger et al. 2015) have proven successful in such tasks.

Furthermore, given that achieving a high signal-to-noise ratio (SNR) is often challenging in astronomical datasets, it is immensely beneficial if additional data can be generated using the available information from the observed sky density distribution and ground-based observations (II data, in our case) of the sources under investigation. Generative Adversarial Networks (GANs), introduced by Goodfellow et al. (2014), have been successful in such data augmentation tasks. Conditional GAN (cGAN) architectures, proposed by Mirza et al. (2014) and applied to a wide variety of datasets by Isola et al. (2017), leverage additional information about the images in the training datasets and have demonstrated remarkable robustness in image recovery across diverse data types.

In the astrophysical context, Schawinski et al. (2017) employed a GAN model to recover features, such as spiral arms, central bulges, and disk structures of galaxies, from noise-affected images. Mustafa et al. (2019) developed and customized a Deep Convolutional GAN, dubbed “CosmoGAN”, capable of generating high-fidelity weak-lensing convergence maps of dark matter distribution that statistically reproduce real weak lensing structures. Coccocini et al. (2021) have successfully generated credible images of planets, nebulae, and galaxies using “lightweight” and “physics-uninformed” GANs to produce synthetic images of celestial bodies. They also generated a “Hubble Deep Field-inspired” wide-view simulation of the universe.

3. INTENSITY INTERFEROMETRY (II) WITH IACT ARRAYS

This section presents a brief conceptual overview of how an array of telescopes is used to perform II obser-

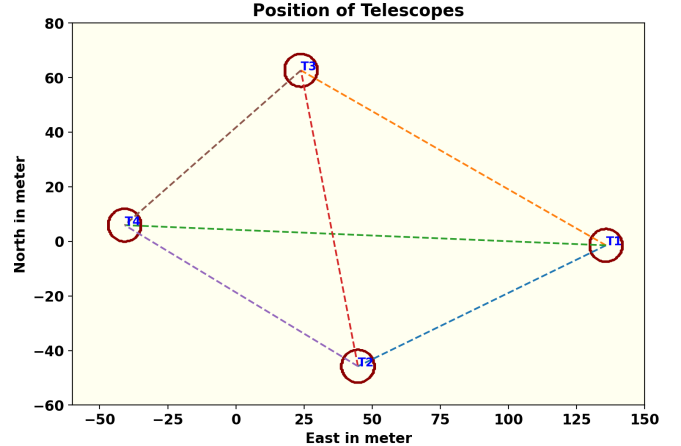


Figure 1. A schematic representation of a hypothetical observation facility with an array of four Cherenkov Telescopes (IACTs) whose relative positions approximately mimic those at VERITAS. This array is used in simulating the II observation of the fast rotators. Each of the telescopes has a diameter of 12m. The baselines provided by the array are of the order of 100m.

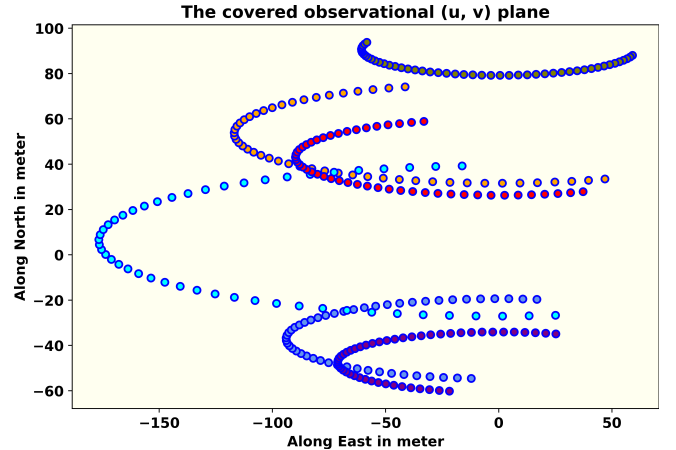


Figure 2. The tracks of the baselines due to Earth rotation (described in sec. 3.3) provided by the hypothetical observation facility of four telescopes arranged in fig. 1 for one night of observation. The number of baselines scales as square of number of telescopes in the array thus leading to greater coverage of the observational plane and better image reconstruction prospects.

vations, and explains the Signal-to-Noise Ratio (SNR) from these measurements.

3.1. The signal for II

As a simple example, let us consider a pair of IACTs pointed at a star. Suppose the two telescopes simultaneously measure the intensity of radiation $I_1(t)$ and $I_2(t)$, respectively. The signals from these detectors are cross-correlated and averaged over time, yielding the second order ($n = 2$) correlation of these intensities as (cf. Ac-

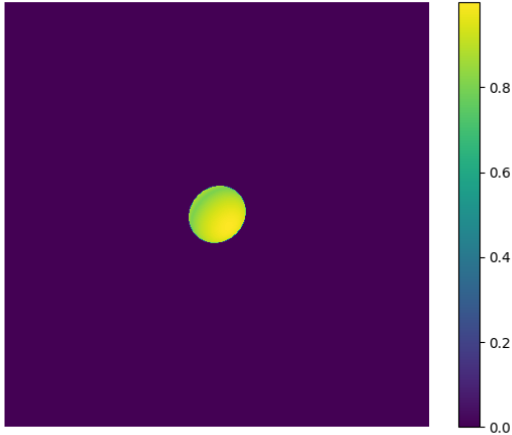


Figure 3. This figure shows one of the simulated fast rotating stars (FRS). The brightness is highest at the poles; gravity darkening visible along the equator. A total of 31460 such images of FRS with different parameter values have been generated to train the model.

ciari et al. 2020; Dravins et al. 2013)

$$g^{(2)} = \frac{\langle I_1(t) \cdot I_2(t + \tau) \rangle}{\langle I_1(t) \rangle \cdot \langle I_2(t) \rangle} \quad (1)$$

where τ is the time delay between the telescopes. For spatially coherent and randomly polarized light, Eq. (1) reduces to the relation (sometimes called the Siegert relation, see e.g., Acciari et al. 2020).

$$g^{(2)} = 1 + \frac{\Delta f}{\Delta \nu} |V_{12}|^2 \quad (2)$$

where Δf is the electronic bandwidth of the photon detectors which measure the intensities and $\Delta \nu$ is the frequency bandwidth of the filters employed in the telescopes to observe the star. Values of $\Delta \nu \sim 1$ THz and $\Delta f \sim 1$ GHz are typical of recent work. In Eq. (2), V_{12} , referred to as the complex visibility function, is the Fourier transform of the source brightness distribution. It contains information about the star's angular diameter. However, the phase information is lost since we measure only the absolute value $|V_{12}|^2$. In observational astronomy, the correlation is often expressed in terms of the normalized contrast, given by:

$$c = g^{(2)} - 1 = \frac{\Delta f}{\Delta \nu} |V_{12}|^2 \quad (3)$$

with $|V_{12}|^2$ being a function of baseline $b = \sqrt{u^2 + v^2}$ on the observational plane (u, v) . This implies the strength of the signal would be enhanced if a larger number of baselines or pairs of telescopes are employed.

3.2. The Signal-to-Noise Ratio for II

The primary purpose of IACTs is to study high-energy gamma rays (with energy $E \geq 30$ GeV) arriving from cosmic sources, entering the Earth's atmosphere, and initiating Cherenkov showers in the upper atmosphere due to multiple scattering. These telescopes feature an array of mirrors that focus light received from a sky source onto their respective set of photo-multiplier tubes (PMTs, see e.g., Aleksić et al. 2016) with appropriate specifications needed for II observations. In the simulation model adopted here, we consider a set of four IACTs, each with similar properties. The positional configuration of these IACTs is shown in Fig. 1. The optical signal directed to a PMT is filtered using a spectral filter with a chosen mean observational wavelength λ and corresponding bandpass $\Delta\lambda$. The use of filters not only reduces background noise but also improves the signal quality and the efficiency of the PMTs. Filtering background skylight becomes even more significant in II observations, as, currently, these are carried out during full moon nights when the primary function of the IACTs (of observing Cherenkov Showers) is rendered infeasible. It is important to note that the light from the stellar source is focused on a PMT attached with each of the telescopes during II observations.

The significance of the signal can be expressed in terms of the signal-to-noise ratio (SNR), which depends on many factors. However, most importantly, it does not depend on the optical bandwidth $\Delta\nu$ of the radiation for a two-telescope correlation. The explanation for the independence of the SNR from $\Delta\nu$ is provided in several works (e.g., subsection 4.1 of Rai et al. 2021). The Signal-to-Noise is given by

$$SNR = A \cdot \alpha \cdot q \cdot n \cdot F^{-1} \cdot \sigma \cdot \sqrt{\frac{T \Delta f}{2}} \cdot |V_{12}|^2 \quad (4)$$

Here, A is the total mirror area, α is the quantum efficiency of the PMTs, q is the throughput of the remaining optics, and n is the differential photon flux from the source. The excess noise factor of the PMTs is represented by F , T denotes the observation time, and σ is the normalized spectral distribution of the light (including filters) (e.g., Acciari et al. 2020).

3.3. Baseline considerations

The measurement of the size of stellar objects via squared visibility depends on the distance between the telescopes, known as the baseline b .

$$|V_{12}(b)|^2 = \frac{c(b)}{c(0)} \quad (5)$$

For achieving a good SNR with a given telescope configuration, covering as much as possible of the interfer-

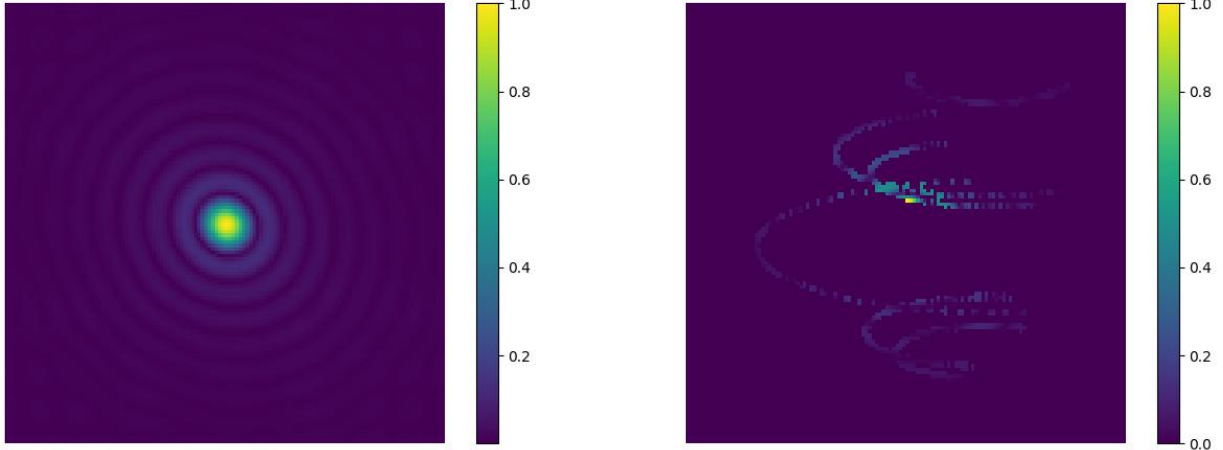


Figure 4. The left panel shows the absolute value of the two-dimensional Fast Fourier Transform of the source depicted in Fig. 3. It represents the intensity interferometric (u, v) plane image of the source that would be obtained by an infinite number of baselines (or an infinite number of telescopes observing the source). The right panel shows the absolute value of the same source measured along the tracks shown in Fig. 2. This figure reflects the sparse nature of the signal received by a realistic finite number of telescopes and baselines sampled from the full (u, v) plane signal space, as shown in the figure on the left panel. Both figures are plotted on a linear scale and normalized to the maximum pixel value in each respective figure.

ometric plane is always desirable. If the source is at the zenith, the coordinates in the Fourier plane (u, v) are given by:

$$(u, v) = \frac{1}{\lambda} (b_E, b_N) \quad (6)$$

where b_E and b_N are, respectively, the baselines expressed in east and north coordinates. However, the sources can be anywhere on the sky, and the telescopes are stationary and may also have different relative altitudes b_A depending on the available terrain. In order to gather maximum possible information on the source during the observation session and to cover as much of the observational plane as possible during such sessions, Earth's rotation must be taken into account using rotated baselines. For a given stellar source with declination δ and hour-angle h , as observed by telescopes located at latitude l , equation (7) provides the rotated baselines for a given pair of telescopes (see e.g., eqs. 8–10 from Baumgartner et al. 2020) with the R -matrices representing the respective rotation operations.

$$\begin{pmatrix} u \\ v \\ w \end{pmatrix} = R_x(\delta) \cdot R_y(h) \cdot R_x(-l) \begin{pmatrix} b_E \\ b_N \\ b_A \end{pmatrix} \quad (7)$$

Fig. 2 shows the track of six baselines generated from the telescopes (Fig. 1) due to the Earth's rotation. Since every pair of telescopes traces an ellipse in the Fourier plane, the total number of ellipses scales as

$$\mathcal{N} = \frac{1}{2} N_T \cdot (N_T - 1) \quad (8)$$

where N_T is the number of telescopes considered. As the number of baselines increases non-linearly, Intensity Interferometry (II) benefits greatly from a large number of telescopes. The CTAO can offer many more baselines — Dravins et al. (2013) considered the telescope configurations then being planned and showed how it would provide a dense coverage of the interference plane.

3.4. A Fictitious Fast Rotating Star: Our Test Case

In our work presented here, we attempt image reconstruction of a fast-rotating star using its simulated Intensity Interferometric observation in a cGAN architecture. Fast-rotating stars are important test cases for understanding various astrophysical processes, including stellar evolution, internal structure, and dynamical behaviour over time. Fast rotation causes stars to adopt an oblate shape, flattening at the poles and bulging at the equator due to the stronger centrifugal force (e.g., Von Zeipel 1924; Maeder 1999). Fig. 3 shows an image qualitatively representing a fictitious fast-rotating star, with brightness (and, therefore, the effective surface temperature) distributed across its surface. The brightness (effective temperature) is highest at the poles and lowest at the equator, a phenomenon known as gravity darkening (Lucy 1967). First direct interferometric detection of stellar photospheric oblateness (of Altair) was pioneered by van Belle et al. (2001) using the Palomar Testbed Interferometer (PTI) and the Navy Prototype Optical Interferometer (NPOI). Gravity darkening due to fast rotation was first observed through interferometric and spectroscopic data from the CHARA Ar-

ray for the fast-rotating star Regulus (McAlister et al. 2005). As pointed out earlier, these two pieces of work, all using Michelson Interferometry, make a subset of several others (van Belle et al. 2001; Domiciano de Souza et al. 2003; McAlister et al. 2005; Domiciano de Souza et al. 2005; Monnier et al. 2007; Pedretti et al. 2009; Zhao et al. 2009; Martinez et al. 2021). The first observation of photospheric oblateness (of γ Cassiopeiae or γ -Cas) using Intensity Interferometry (II) has been recently carried out at VERITAS observatory and is reported by Archer et al. (2025). Reportage of such observations of other γ -Cas like targets and other class of FRS by Cherenkov Telescope arrays, such as the MAGIC array, are expected by 2026. In addition, observation and measurement of gravity darkening using II is the natural next step and is yet to be reported. In this context, our work of reconstructing the image of FRSs from their II-simulated observations using cGAN is an attempt at solving this inverse problem along with mitigation of loss of phase information in II.

II counts the photons arriving at the telescopes from the stellar object. The correlation of these photon arrivals at the telescopes yields the squared visibility Eq. (5), as explained in subsection 3.1. The left panel of fig. 4 shows the signal from the source shown in Fig. 3 using II, displayed on linear scales. A point to note here is that this figure represents the signal from the source that would be recorded by an infinite number of baselines provided by an infinite number of telescopes on the interferometric plane. In practice, only a small part of this information is available (as seen in right panel of Fig. 4), because one has a finite number of baselines corresponding to the finite number N_T of telescopes at our disposal and a limited observation schedule. We have simulated the II observation of the fictitious star by a hypothetical observation facility having an array of four IACTs with their relative positions approximating those at VERITAS (correlated with baselines as seen in Fig. 1) over one night. Using this modest amount of signal from one night’s observation, we have trained a cGAN to construct the image of the source.

4. GENERATIVE ADVERSARIAL NETWORKS

Generative Adversarial Networks (GANs) were introduced by Goodfellow et al. (2014). A GAN model involves two competing deep neural network models, referred to as the Generator and the Discriminator. These two networks engage in a zero-sum “Minimax” game, as in Game Theory. Given a real data set $\{x_i\}$ (for example, a set of real images) drawn from some unknown distribution $P_{\text{data}}(x)$ generated by some unknown or ill-understood process, the objective here is to generate

a new set (of images) whose probability distribution should match $P_{\text{data}}(x)$ as closely as possible. During the training of the two models, the Generator samples a latent variable z from a known prior distribution $P_z(z)$ (*e.g.*, the Normal Distribution) and produces a synthetic sample $G(z)$ to start with and, subsequently, based on updates received from the Discriminator as its training progresses. The Discriminator, being a probabilistic binary classifier, receives either a real data sample x or a generated sample $G(z)$, and outputs a probability that the input is real. The Discriminator aims to maximise its classification accuracy, while the Generator aims to fool it by trying to minimize it. The training of these two networks proceeds alternately leading to the optimization of the adversarial loss function $L(D, G)$ given by

$$\begin{aligned} L(D, G) &= \min_G \max_D V(D, G) \\ &= \mathbb{E}_{x \sim p_{\text{data}}(x)} [\log D(x)] \\ &\quad + \mathbb{E}_{z \sim p_z(z)} [\log (1 - D(G(z)))] . \end{aligned} \quad (9)$$

The two neural networks $G(z) \equiv G(z; \theta_G)$ and $D(x) \equiv D(x; \theta_D)$ are parameterized by θ_i with $i = G$ or D respectively. During its training, the Generator generates the differentiable function $x_{\text{gen}} \equiv G(z)$ that maps z to the data space x . Through such maps the Generator generates its own distribution $p_G(x_{\text{gen}})$ and through the training episodes, specifically by iteratively updating its parameters θ_G , aligns this distribution with the distribution of real data $p_{\text{data}}(x)$. The training data set provided to the Discriminator is constructed by mixing real data points x and generated data points x_{gen} in equal ratio. The Discriminator generates the function $D(x)$ that represents the probability that x originates from real data. Eq.(9) implies that training of the GAN model moves towards maximization of the expectation of $D(x)$. Through this process, both the parameters θ_G and θ_D are optimized such that $p_G(x_{\text{gen}})$ gets maximally aligned with $p_{\text{data}}(x)$.

For a given fixed Generator $G(z)$, the problem can be reformulated as:

$$\begin{aligned} \max_D V(D, G) &= \mathbb{E}_{x \sim p_{\text{data}}} [\log D_G^*(x)] \\ &\quad + \mathbb{E}_{x \sim p_G} [\log (1 - D_G^*(x))] \end{aligned} \quad (10)$$

where D_G^* denotes the optimum of the discriminator. As seen in equation (11), the global optimum of equation (10) is achieved if and only if $p_G = p_{\text{data}}$. Furthermore, if both G and D are allowed to reach their respective optima, – the so called Nash point of the Minimax game – p_G converges to p_{data} .

$$D_G^*(x) = \frac{p_{\text{data}}(x)}{p_{\text{data}}(x) + p_G(x_{\text{gen}})} \quad (11)$$



Figure 5. An illustrative example of the input used for training the cGAN model. The picture on the left shows the source image, which serves as the ground truth or the real data (x), as mentioned in the Flow Diagram (Fig. 6 discussed later during the training). The picture on the right represents the simulated II observation pattern of the source (on the left) using a hypothetical observation facility having as array of four IACTs (see Fig. 1) and the tracks of the six telescope baselines (see Fig. 2) generated by these four IACTs due to Earth’s rotation during the observation session. This pattern referred to as y , in the Flow Diagram (Fig. 6 discussed later) forms the “condition” during the training to which the GAN model has to conform. Salt-and-pepper noise is added to this pattern for enhancing the robustness of the cGAN model. Together, these images form a training pair, where the GAN learns to reconstruct a predicted image (modeling of observed signal) similar to ground truth (left) from the noisy baseline signal (right). The grayscale in both images is normalized to the brightest pixel.

At this point, the Discriminator finds its job no better than random guessing. A more comprehensive discussion of the problem, including proofs, is provided in Goodfellow et al. (2014).

Subsequently, the GAN framework was extended to a conditional model (Mirza et al. 2014). This new model, known as “conditional GAN” or cGAN injects a conditioning variable y into both networks: the Generator now generates $G(z | y)$, and the Discriminator evaluates $D(x | y)$. The adversarial objective becomes

$$V(D, G) = \mathbb{E}_{x, y \sim p_{\text{data}}(x)} [\log D(x|y)] + \mathbb{E}_{z, y \sim p_z(z)} [\log (1 - D(G(z|y)|y))] \quad (12)$$

The conditional variable y in a cGAN can be various additional information including images, labels or text contextual to “ground truth” real data x . Among various types of cGANs, Pix2Pix GAN with its image-to-image translation design is suitable for the task at hand. In our work, we specifically use this conditional variable by choosing y to represent the ground-based intensity-interferometry (II) observation patterns: the Generator is trained to produce stellar surface images that not only look realistic but also conform to the measured II correlations, while the Discriminator judges realism *and* consistency with the II data.

Isola et al. (2017) further observed that combining the cGAN from Eq. (12) with the traditional $L_1(G)$ loss (also known as the Mean Absolute Error) improves the results, as the Generator is encouraged to produce outputs closer to the target image in a pixel-wise sense. We adopt this approach in the training of our cGAN model by including $L_1(G)$ defined in eq.(13)

$$L_1(G) = \mathbb{E}_{x \sim p_{\text{data}}, z \sim p_z(z)} [\|x - G(z | y)\|_1]. \quad (13)$$

The total adversarial loss function, along with the L_1 loss modulated by a hyperparameter λ then becomes

$$L_{\text{tot}} = \arg \min_G \max_D V(D, G) + \lambda \cdot L_1(G). \quad (14)$$

This type of network has demonstrated remarkable robustness across a variety of applications. For example, it can generate colored images from grayscale inputs based on architectural labels, transform images from day to night, and even predict maps from satellite data. A more extensive list of applications is provided in Isola et al. (2017).

4.1. Generator

As discussed above, in a GAN the Generator, a deep neural network in itself, is responsible for producing synthetic data, in this case, images that resemble those

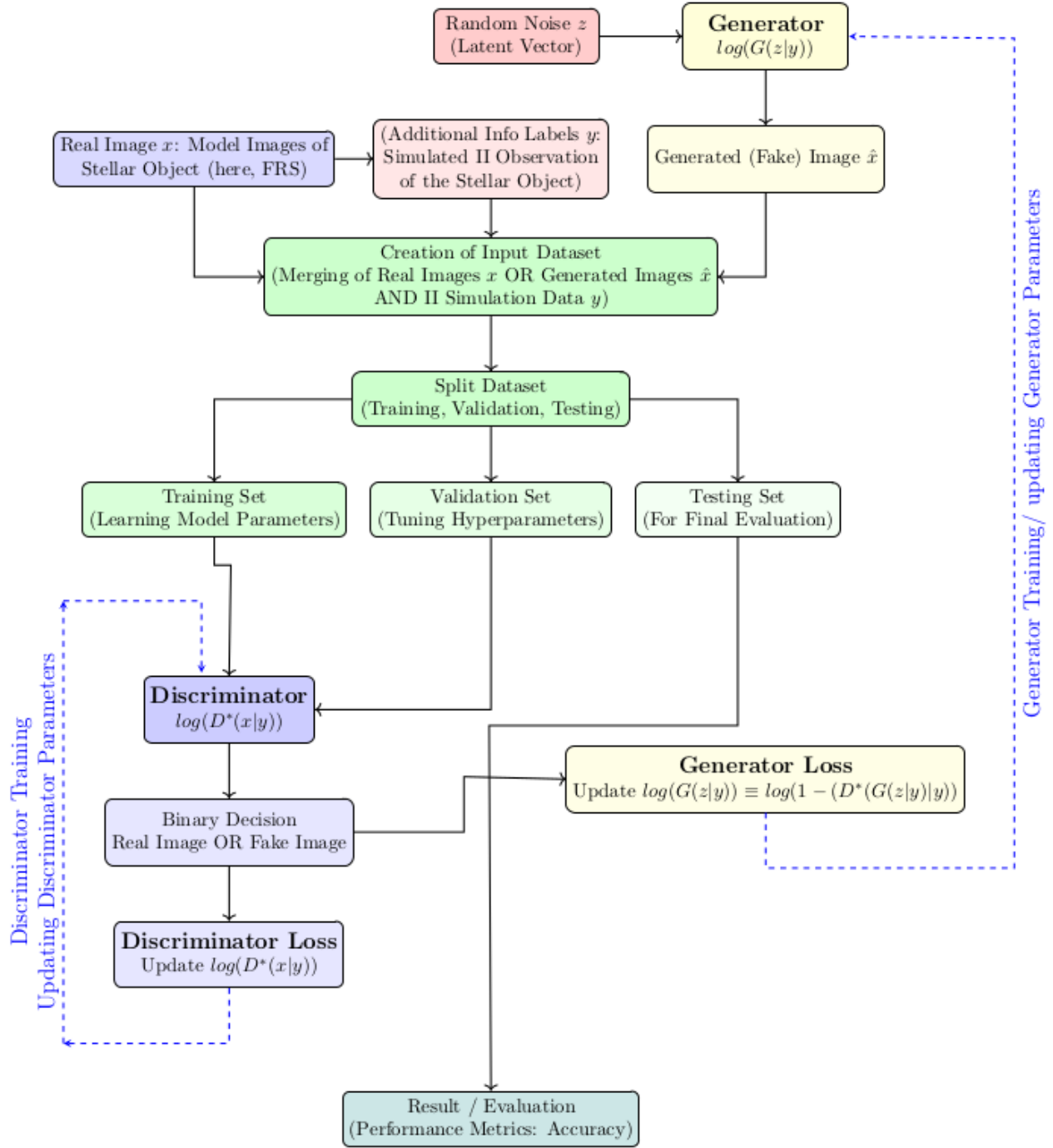


Figure 6. A schematic representation of the features of a cGAN model used in this work and the iterative process of its training, validation and testing. The process constitutes four broad stages: (1) choice of an appropriate GAN architecture including both the Discriminator and the Generator (not shown in this figure) (2) preparation of the Training, Validation and Testing datasets and (3) Training and Validation of the Model (4) Testing and Evaluation of the Model. The stages (2), (3) and (4) are depicted in this figure. The datasets are prepared in three broad steps: (i) generating the “ground truth” images of fictitious fast-rotators x , the sparse II images y used as the “condition” images in the Model and the generated images z sampled from a Normal Distribution (ii)merging these images into individual files with $(x|y)$ and/or $(z|y)$ (as seen in an illustrated sample in Fig.(5)) and generating the full dataset in this process, and finally (iii) partitioning the full dataset into Training Set, Validation Set and the Testing Set. After the iterative training of the Model and its validation process is complete (“Nash point” of the Minimax Game is reached), the Model is tested using the Testing Set and evaluated.

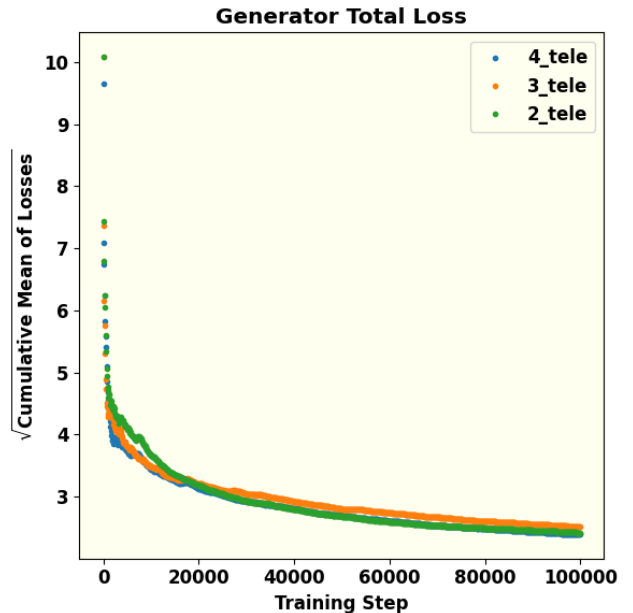
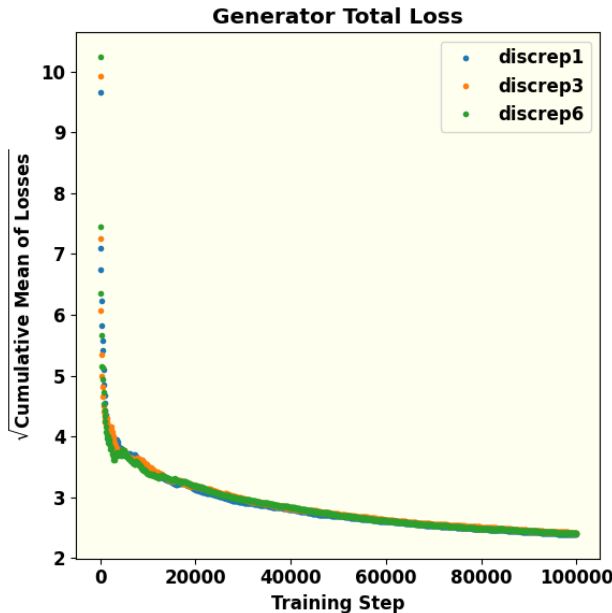
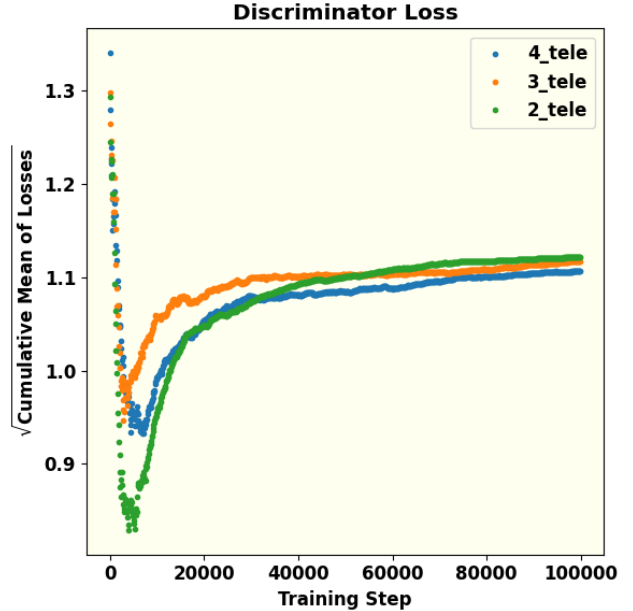
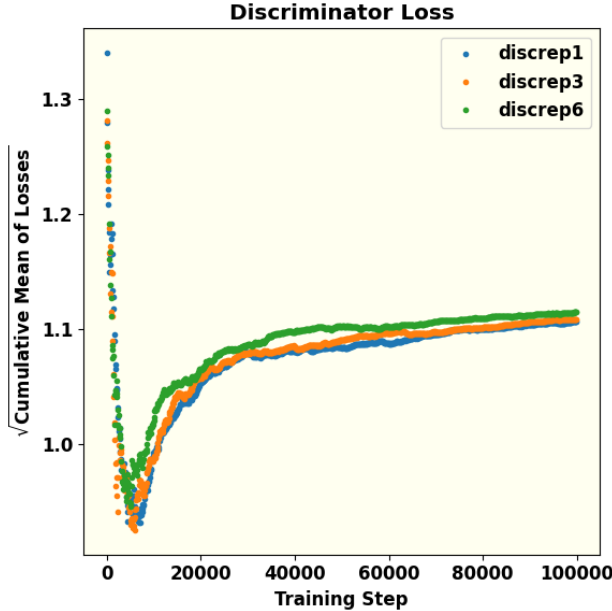


Figure 7. These figures show the effect of the ratio of episodes of Discriminator training per every episode of Generator training. This hyperparameter is termed Discriminator repetition or (discrep) in the figures. The square root of the cumulative mean of the losses are plotted against the training steps for 3 values of this ratio. Understandably, this ratio has a higher impact on the Discriminator loss than the Generator loss. Equal number of episodes of training produces minimum cumulative loss of the Discriminator. The dip in the Discriminator loss during the initial phases of its training can be interpreted as its early success in detecting “fake” (or generated) images because of a poorly trained Generator. With gradual training of the Generator, the success rate of the Discriminator decreases and eventually approaches saturation with equal probability of being successful in telling “fake” from real. The continual decrease and eventual saturation of the Generator loss is a result of its training to generate better images with increasing number of steps.

Figure 8. The square root of cumulative mean of Discriminator and Generator loss for different numbers of telescopes. The number of telescopes is also another hyperparameter that has significant impact on the model performance. If there are only two telescopes, both Discriminator and Generator are not trained smoothly. The result of four telescopes is a lot better because the cumulative mean of loss functions is smaller compare to other parameters. For the same reasons as explained in Fig.(7), we observe initial dip and eventual saturation of the Discriminator loss and continual decrease and eventual saturation of the Generator loss with training steps.

of a fast-rotating star. In this work, the Generator is implemented as a U-Net convolutional network (Ronneberger et al. 2015). The U-Net consists of a symmetric encoder-decoder structure forming a characteristic “U” shape along with skip connections: the left (contracting or down-sampling) path, the right (expanding or up-sampling path) and the connecting (bottle-neck) path. The left down-sampling path repeatedly applies 3×3 convolutions (padded to preserve spatial dimensions) followed by LeakyReLU activations and strided convolution (with stride of 2), by progressively halving the spatial resolution while doubling the channel depth (typically $64 \rightarrow 128 \rightarrow 256 \rightarrow 512 \rightarrow 1024$). At the bottleneck, high-level features are processed without further spatial reduction. The right up-sampling path mirrors this process using 2×2 transposed convolutions (stride 2) for up-sampling, halving the channel count at each level and using ReLU as the activation function for all its layers except the output layer. Additionally, a dropout layer is introduced at the beginning of the upsampling phase to mitigate overfitting of the Generator model (Isola et al. 2017). Critically, long skip connections concatenate feature maps from each encoder (down-sampling) level to the corresponding decoder (up-sampling level), directly injecting high-resolution details into the reconstruction process. This enables the network to “remember where everything is” while the deep bottleneck still provides the large receptive field needed to think globally about image structure and semantics. Besides the strided convolutions, modern variants of U-Nets used in state-of-the-art GANs incorporate residual blocks within resolution levels, and frequently add spectral normalization and self-attention at the bottleneck for improved training stability and long-range dependency modelling. These architectural choices allow our U-Net generator to simultaneously recover sharp, high-frequency details (stellar limb edges, limb-darkening profiles, gravity darkening, and rapid-rotation-induced oblateness) and enforce global coherence (overall disk morphology and physical consistency with the observed interferometric visibilities)—making it ideally suited for high-fidelity sky-image reconstruction of fast-rotating stars from sparse ground-based intensity interferometry observations.

During the training, the total Generator Loss function L_G including the L_1 loss defined in eq.(13) that is minimized is given by

$$\begin{aligned} L_G = & -\mathbb{E}_{z \sim p_z(z)} [\log D(G(z | y) | y)] \\ & + \lambda \mathbb{E}_{x \sim p_{\text{data}}, z \sim p_z(z)} [\|x - G(z | y)\|_1]. \end{aligned} \quad (15)$$

Here,

- x denotes a real data sample (e.g. the “ground-truth” image; here, the synthetically generated fast rotator image) corresponding to condition y , the simulated II observation data.
- z is a random latent vector drawn from the prior $p_z(z)$.
- $G(z | y)$ is the generator output (the reconstructed / synthesized image) given z and condition y .
- $D(\cdot | y)$ is the discriminator’s estimate (probability) that its input is “real,” given the same condition y .
- λ is a hyperparameter controlling the trade-off between adversarial realism and pixel-wise fidelity (typical values depend on the problem, e.g. in pix2pix, $\lambda = 100$).

4.2. Discriminator

The Discriminator is tasked with classifying the images produced by the Generator as either real or fake. It takes a real image from the dataset (often referred to as the target image for the Generator) and provides feedback to guide the Generator toward producing more accurate images. In this work, the PatchGAN model (Isola et al. 2017) is employed as the Discriminator. Unlike a traditional global classifier, PatchGAN evaluates individual patches of the image, outputting a grid of predictions rather than a single scalar value. Each element in the grid corresponds to the “realness” of one patch of the image under examination of the Discriminator at a time. The final loss of the Discriminator is the average over all the patch responses. Evaluating the “realness” of the input image in terms of its constituent patches facilitates capture of texture/ style and other high frequency components in the image. As compared to a global discriminator, it also reduces the number of parameters in the network thereby helping reduce computation cost. It also works on images with arbitrary sizes.

Prior to the down-sampling of data using PatchGAN, each input image is preprocessed with application of Zero Padding followed by batch normalization. The purpose of Zero Padding is to prevent the loss of spatial information and to facilitate the extraction of deeper features from the down-sampled output. Batch normalization is required to stabilize the learning (loss minimization) process. PatchGAN then reduces the spatial dimensions of the images to extract localized features, ensuring the model focuses on smaller regions. In this down-sampling stage, a leaky version of the Rectified Linear Unit (LeakyReLU) is applied in the convolutional

602 layers, similar to the approach used in the Generator.
 603 The probability $D(\cdot|y)$ that the patch of the input im-
 604 age represented by \cdot is “real” is evaluated through this
 605 process. The loss function D of the full input image is
 606 obtained by averaging over all the patch responses.

607 The Discriminator Loss function L_D that is optimized
 608 during the training process is given by

$$609 \quad L_D = -\mathbb{E}_{x \sim p_{\text{data}}(x|y)} [\log D(x|y)] \\ - \mathbb{E}_{z \sim p_z(z)} [\log (1 - D(G(z|y)|y))] \quad (16)$$

610 where the arguments of the D and G functions are as
 611 noted in the text following eq.(15) This loss is composed
 612 of two parts: one that assesses how accurately it iden-
 613 tifies fake images (by comparing predictions to a target
 614 value of 0) and the other that measures how accurately
 615 the Discriminator identifies real images (by comparing
 616 predictions to a target value of 1).

617 The training procedure of these two components of
 618 the cGAN model can be outlined as follows:

- 619 • The discriminator D is updated by minimizing
 620 L_D , keeping G fixed (so that D becomes better
 621 at distinguishing real vs generated images).
- 622 • The generator G is updated by minimizing L_G ,
 623 keeping D fixed, thus pushing G to generate im-
 624 ages that are (a) judged “real” by D , and (b) close
 625 (in pixel-wise sense) to the ground-truth x .

626 5. NETWORK PARAMETERS

627 An appropriate cGAN architecture along with a set of
 628 hyperparameters was optimized by tuning. The objec-
 629 tive of the model, as already mentioned, was to learn to
 630 faithfully reproduce a set of sky-images of fast rotators
 631 subject to the condition that those images are consistent
 632 with their simulated II observation data. We discuss
 633 below the architecture and the hyperparameters of the
 634 cGAN model used for this task. Given the adversarial
 635 nature of GANs, where the Generator and Discrimina-
 636 tor engage in a minimax game, careful tuning of key
 637 parameters is critical to ensure that both networks are
 638 well-balanced for effective training.

639 5.1. Data Preparation

640 First, we generate synthetic images of rapidly rotating
 641 stars by modelling them as oblate spheroids with vary-
 642 ing radii and oblateness parameters between 0.5 and 1.
 643 To incorporate the effect of gravity darkening, we also
 644 consider different viewing angles and assume a linear de-
 645 pendence on the declination angle of each point on the
 646 stellar surface. The traced ellipses result from integrat-
 647 ing over the source’s hour angle.

648 Next, Salt and Pepper noise is introduced into these
 649 images; usually this is done at the rate of 0.5% of the
 650 number of pixels in the image. Then, the images are re-
 651 sized and their mean is subtracted. A two-dimensional
 652 Fast Fourier Transform, along with a Fourier shift, is ap-
 653 plied, yielding a complex number for each pixel. Since II
 654 does not measure phase, the absolute value is calculated.

655 Next, sampling of the interferometric plane is in-
 656 troduced via pixel-wise multiplication of the absolute-
 657 valued Fourier-transformed image (left panel of Fig. 4)
 658 and the baseline tracks of (Fig. 2) generated by the four
 659 IACTs due to Earth rotation during the II observation.
 660 The result is a map in the Fourier plane featuring several
 661 ellipses, which is also referred to as the sparse sampling
 662 map (right panel of fig. 4). This map represents the
 663 sparse sampling of the signal space corresponding to the
 664 source (Fig. 3) observed with four telescopes (Fig. 1).
 665 In essence, the right panel of fig. 4 represents the result
 666 of simulated II observation of the fictitious fast-rotator
 667 illustrated in fig. 3.

668 Finally, we normalize the pixel values and convert
 669 them to 8-bit integers, producing an image that encodes
 670 the sparsely sampled, phase-free visibility measured by
 671 II. The image of the corresponding simulated (fictitious)
 672 star, which serves as the “ground truth” is processed
 673 identically to avoid any bias. These two images are
 674 merged side-by-side into a single image (as shown in
 675 Fig. 5). The dataset thus created is split into three
 676 parts in the proportions of 80% for training, 10% for
 677 validation, and 10% as the test set. This partition of
 678 the full dataset is indicated in the Fig.6. In the follow-
 679 ing, we refer to these three parts as the Training Set,
 680 the Validation Set and the Testing Set respectively.

681 5.2. GAN Architecture

682 The GAN architecture used in this work is a Pix2Pix
 683 cGAN, which uses an image-to-image translation strat-
 684 egy with both the ground truth and the condition being
 685 images. Originally introduced by Isola et al. [Isola et al. \(2017\)](#), this architecture is specifically suitable for image
 686 processing and reconstruction objectives. For instance,
 687 the TensorFlow tutorials⁶ demonstrate its application to
 688 a dataset of architectural facades. This architecture has
 689 been adapted for the phase retrieval problem at hand
 690 here. The network is implemented using the TensorFlow
 691 library ([Abadi et al. 2016](#)), calculations are performed
 692 with `scipy` ([Virtanen et al. 2020](#)), and plots are gener-
 693 ated with `matplotlib` ([Hunter 2007](#)).

⁶ <https://www.tensorflow.org/tutorials/generative/pix2pix>

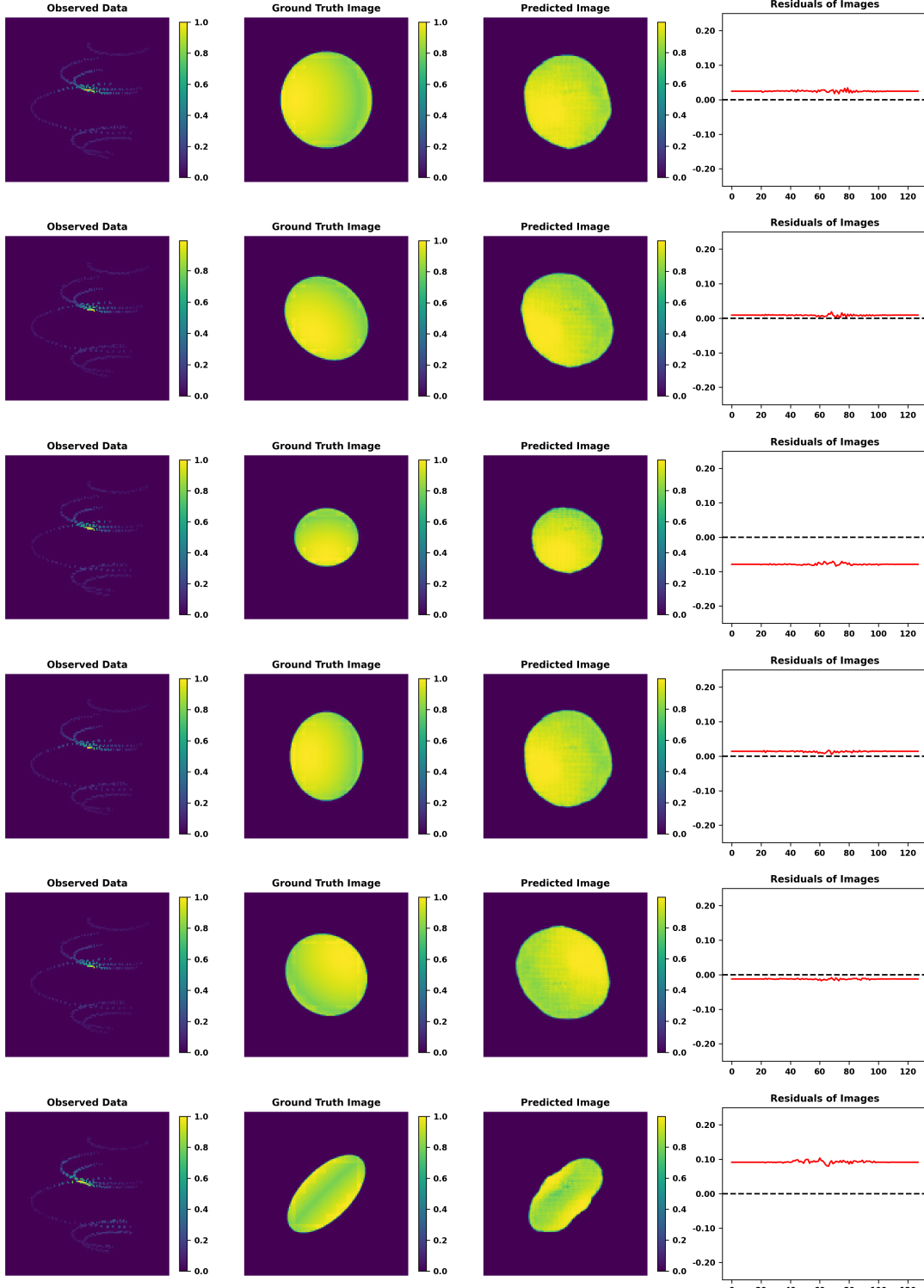


Figure 9. Example results of image reconstruction using the cGAN model along with the II observations simulated in this work. Each row in this figure represents the results for a hypothetical fast-rotating star. The left panel represents the sparse II pattern obtained by the simulated observation of the star using the four IACTs illustrated in Fig.1. This image acts as the “condition” part of the data input to the cGAN model. The second panel from left displays the real image, or ground truth, which the Discriminator uses to distinguish from the images generated by the Generator. The data generated for training, validation and testing of the cGAN model is a merge of this image and its II pattern presented in the left panel. The third panel is the reconstructed image, or the predicted image, produced by the trained GAN model . The fourth and the last panel is the difference between the ground truth and the predicted image in the (u, v) plane.

5.3. Hyperparameter Tuning

The cGAN model architecture used in this work employs several hyper-parameters, which are explained briefly below (for a more in-depth discussion, see Murphy 2022).

The learning rate (lr) of the optimizer determines how much the model updates its parameters with each iteration. A learning rate that is too small may lead to underfitting, while one that is too large can render the model unstable. Therefore, selecting an appropriate learning rate is crucial (Murphy 2022). A canonical choice in Pix2Pix and other GAN models is $lr = 2 \times 10^{-4}$. In our case too, we found this choice to be appropriate.

The kernel size refers to the dimensions of the convolutional kernel used in the network, determining how many pixels are combined to produce a new pixel. A larger kernel size can capture features spanning several pixels, but it may also incorporate unrelated features. Small kernel sizes are preferable in cases where target images finer details or high spatial frequency features. Since the “ground truth” target images in our case have longer scale gravity darkening features, we have opted for the more canonical choice of kernel size being 5.

The amount of noise is controlled by two parameters, “alpha” and “beta”, which indicate the percentage of pixels altered to either white or black, hence the term Salt and Pepper noise. Here, “alpha” is applied to the real image, while “beta” is applied to the generated image. Different ratios (“alpha/beta”) can lead to varying model performance; however, our results indicate that distinct noise rates do not significantly affect the loss functions.

The batch size defines the number of images processed simultaneously by the network. Smaller batch sizes have been observed to improve generalization (Prince 2023). However, because a larger batch size significantly increases training time, a batch size of 1 is used. Besides, in Pix2Pix cGAN implementations found in literature this choice is found to be often preferred.

The buffer size of a Pix2Pix GAN refers to a small memory of image pool of previously generated images. They are occasionally fed to the Discriminator in place of the freshly generated ones. This strategy of mixing old and new fakes mitigates the risk of mode collapse wherein the Discriminator tends to map all or large number of generated images to only one or a few real “ground truth” image(s). We have chosen a fairly large buffer size (=1400) to protect the model against mode collapse.

In the training of GANs, one often-followed strategy to potentially boost performance is to give the Discriminator an advantage by increasing its number of train-

ing epochs before returning to the Generator’s training. This hyperparameter is referred to as the Discriminator repetition (as seen in Table 1). While this can lower the Discriminator loss, as shown in Fig. 7, it also increases training time. In training our model, we did not notice any significant advantage derived from this strategy. Since the generated images did not noticeably improve with additional Discriminator training, we adopted the strategy of training both the networks with equal preference (Discriminator repetition = 1).

One domain specific hyperparameter of the cGAN model presented here is the Number of Telescopes N_T . The degree of sparse sampling of the intensity interferometric (II) image plane can be varied to provide the model with access to more number of active (non-zero) pixels. Point to note here, is that the coverage of the Fourier interferometric plane (number of active pixels in the II image) scales with available number of baselines, and the latter scales quadratically with the number of telescopes. Fig. 8 shows the loss functions for different numbers of telescopes. There is a significant disparity in performance of the model: at the “Nash point”, both the loss functions are minimized for the case of four telescopes. Overall, the degree of sparse sampling appears to have the most pronounced effect of all the hyperparameters.

The hyperparameter Output Channels refers to the number of channels in the generator output (e.g., 1 for grayscale, 3 for RGB). It is worthwhile to recall that the cGAN model constructed in this work is trained on “ground truth” target images and the simulated II data, both in grey scales as seen in Fig. 5. It is natural that the output of this model will be in grey scales only. Therefore the value of this hyperparameter is set to 1. The choice of hyperparameter λ has been commented upon earlier.

An optimized set of hyperparameters is selected through an iterative process of training and validation. For a tentatively chosen set of the hyperparameters, the model is trained using the Training Set until the both the Discriminator and the Generator loss functions are minimized. This model, thus trained along with its model parameters, is then passed through validation using the Validation Set. This cycle of training and validation is iterated till an optimal set of hyperparameters is arrived at. During each epoch of training of the model, both the Discriminator and the Generator networks are trained for 100,000 steps. Plots of the “Discriminator Loss” function and the “Generator Total Loss” function presented in Fig. 7 and Fig. 8 represent the results of this training for two of the hyperparameters, namely, the Discriminator repetition (“discrep”, in

short) and the Number of telescopes, respectively. Obviously, the most compute-intensive part of this process is that of the training of the Model. The results of training and validation presented in this work were carried out on a CPU using two nodes, each with 48 threads and the entire process of training and validation required approximately 20 hours on the machine employed for this work. This iterative process of training and validation of the Model is represented schematically in the Fig.6. The chosen optimal set of hyperparameters is presented in the table Table-1. This optimized and trained Model

Table 1. Selected hyperparameters used for training the model.

Hyperparameter	Value
Learning rate	2e-4
Kernel size	5
Alpha/Beta	1
Batch size	1
Buffer Size	1400
Discriminator repetition	1
Number of Telescopes	4
Output Channels	1
Lambda	100

is then subjected to testing and evaluation using the Testing Set. The results of this testing and evaluation is presented in the following section.

The Pix2Pix cGAN architecture along with the choice of the values of the hyperparameters mentioned in the Table -1 and used in the implementation of this architecture constitutes the cGAN model (hereinafter referred to as “the GAN Model” or simply “the Model”).

6. IMAGE RECONSTRUCTION: RESULTS AND EVALUATION

In this section, we examine the performance of the GAN Model whose architecture and choice of hyperparameters have been discussed above. We subject the trained Model to the task of phase retrieval and image reconstruction on the Testing Dataset.

6.1. Visual Evaluation of Images Predicted by the Model

Fig. 9 demonstrates the success of the trained Model in reconstructing the images of a sample of the fictitious fast-rotators drawn from the Testing Set.

The four panels from left to right in each row of Fig. 9 represent the following:

- The left panel represents the sparse II pattern obtained by the simulated observation using the four

IACTs illustrated in Fig.1. As explained earlier, this image acts as part of the input, namely its “condition” part. This image acts as the condition that the sky-images of the star generated by the Generator must conform to.

- The second panel from left displays the real image, or ground truth target image, which the Discriminator loss function uses to distinguish from the images generated by the Generator.
- The third panel from left presents the reconstructed (or predicted) image corresponding to the ground truth (second panel) and generated by the trained Model. The similarity of these two images indicates the success of the Model in its stated objective of image reconstruction. We remark that rotating the images by 180° would not change the data. That is, each predicted image contains an arbitrary choice among two possible orientations, differing by 180° .
- The right panel shows the residuals between the ground truth target image and the predicted image in the interferometric plane. The small values are indicative of the success of training the Model.

The predicted images and the residuals presented in the third and the fourth columns (from left) of Fig. 9 show encouraging results, conveying visual information about the source’s size, shape, and brightness distribution across its surface fairly accurately. This has been achieved on the basis of the input provided by II observation using only six baselines, corresponding to four telescopes, at present the maximum on which II is already implemented. Further improvements could surely be achieved by increasing the number of telescopes to enhance the coverage of the (u, v) plane. A closer examination of this proposition might be able to contribute to the design and instrumentation aspects in the existing and upcoming CTAO.

6.2. Evaluation of the Model using Moments

The reconstructed images are visually compelling, demonstrating the Model’s effectiveness in using II to reconstruct images. However, visual assessment alone is insufficient; statistical evaluation of the generated images in comparison with the ground truth images is necessary to validate the results. We present here the results of our calculation and comparison of the moments of distribution pixel brightness in the target “Ground Truth” images and the “Predicted” images.

Image moments capture key properties of the reconstructed objects, such as shape, size, and intensity dis-

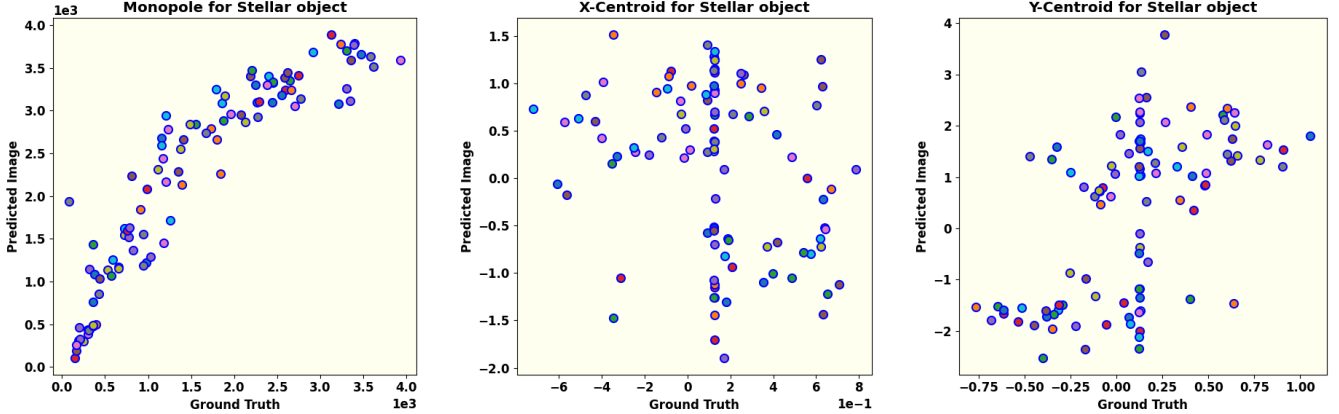


Figure 10. This set of figures shows comparisons of the monopole, and the coordinates of the centroids (x_c, y_c) of the pixel brightness distribution of the ground truth images and the corresponding images predicted (generated) by the trained model. The monopole moment of the images represents the overall pixel brightness of the images. The values, as expected of a trained Model, not only lie in same range, but lie close to the diagonal and show an approximate equality. The centroids of both the ground truth images and the predicted images lie within small ranges of pixel values as should be expected of an ideally trained model. Please see the relevant text for detailed comments.

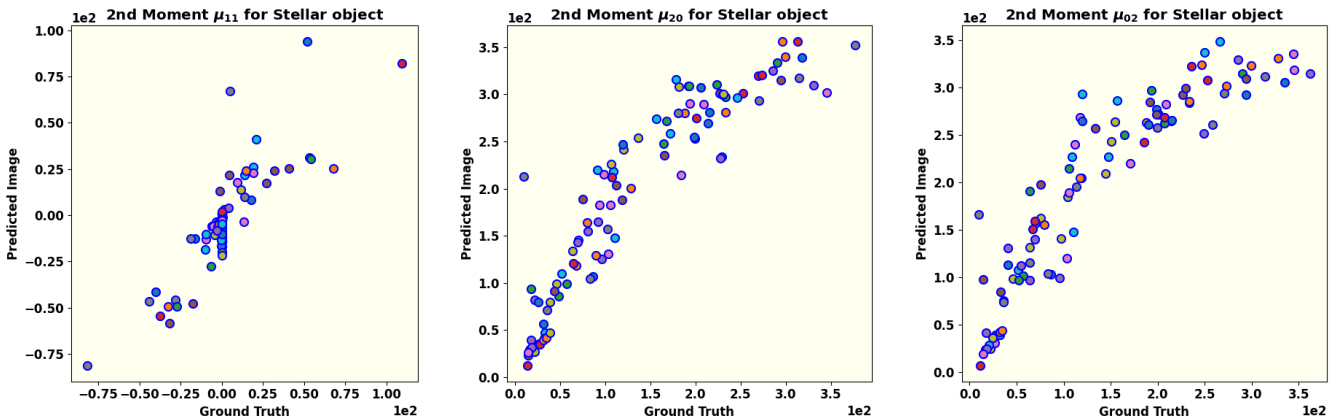


Figure 11. The second order central moment of the brightness distribution of the images is analogous to the moment of inertia of a mass distribution. The panels of this figure show the comparison of the second order moments (μ_{11}, μ_{20} , and μ_{02}) of the predicted images vs. the ground truth images from left to right respectively. Approximate equality of these moments is evident. The small scatter in the moments of the predicted images is indicative of a balanced training of the Model.

tribution, by quantifying features like position, orientation, and brightness distribution. By comparing the moments of the Model-generated images with those of the ground truth, we can objectively assess the consistency and accuracy of the reconstruction. This approach provides a reliable framework for evaluating reconstruction quality, as image moments can reveal subtle differences in geometric and intensity properties that might not be apparent through visual inspection alone.

The raw moment M_{ij} of an image is defined as (Hu 1962)

$$M_{ij} = \sum_x \sum_y x^i y^j I(x, y) \quad (17)$$

where $I(x, y)$ represents the intensity at pixel (x, y) . The zeroth order raw moment, or monopole, represents the total intensity of an image. It is computed by summing all pixel values across the image, yielding an overall intensity measure. In this context, analyzing the monopole provides the total pixel brightness of the images of the fictitious stars. According to Eq. (17), the monopole of an image is calculated as:

$$M_{00} = \sum_x \sum_y I(x, y). \quad (18)$$

An ideally trained Model should predict the overall pixel brightness of the generated images to be in the same range of values, if not equal to those of the ground truth images. The left panel of Fig. 10 displays the

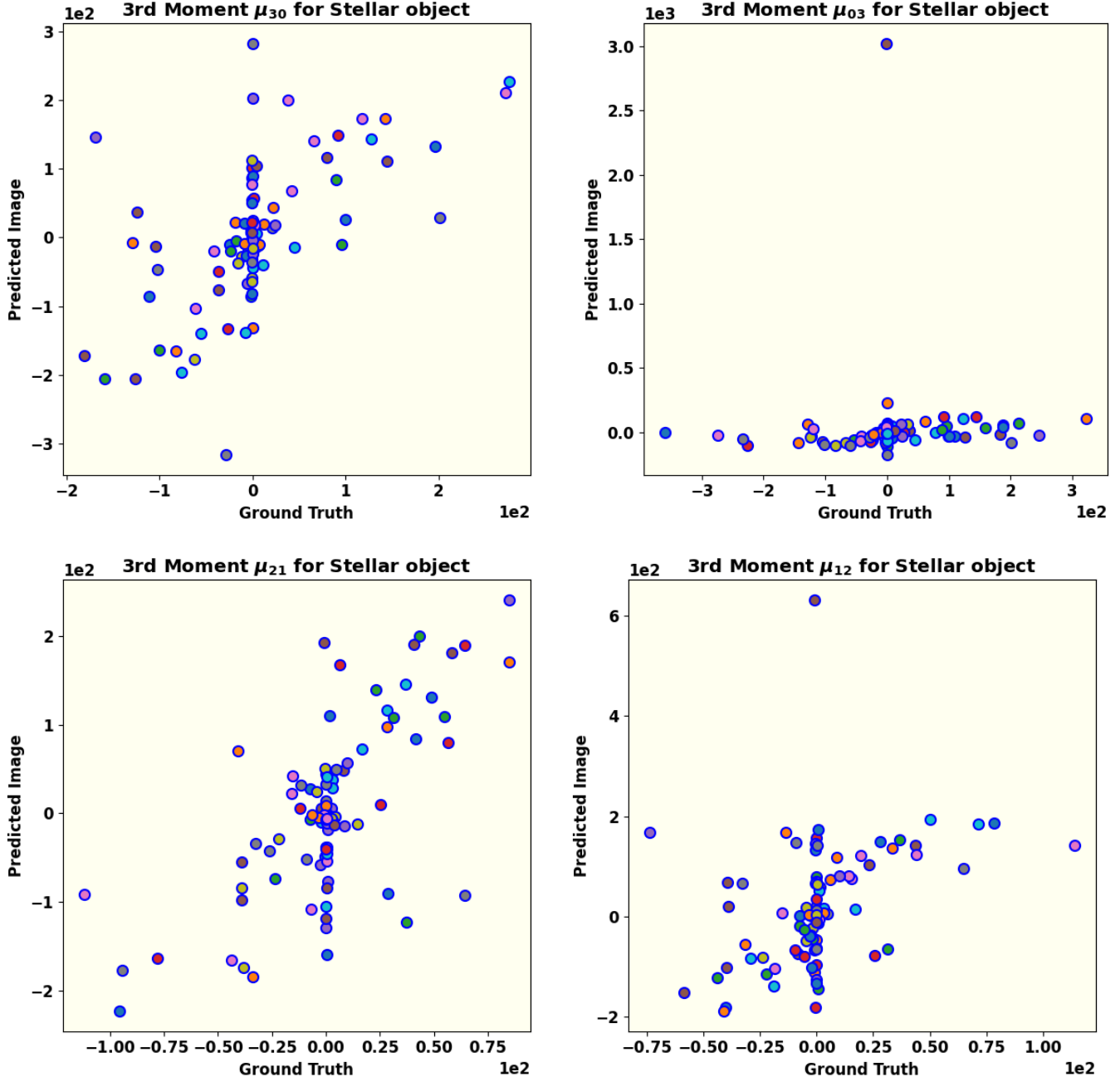


Figure 12. Shown here are all the third-order central moments (μ_{30} , μ_{03} , μ_{21} , and μ_{12}) for ground truth and predicted images generated by the trained Model. They represent the skewness of the brightness distributions. The low skewness in the brightness distribution of the ground truth images is evident. One outlier among the predicted images dominates their skewness distribution along the y -axis as seen in the values of μ_{03} and μ_{12} . The trained Model, however, seems to have learned the approximately uniform distribution of skewness along the x -axis as is evident, with a few outliers though, in the values of μ_{30} and μ_{21} .

monopole values for 100 reconstructed images. The plot reveals a broad agreement in the overall intensity of the ground truth targets and the predicted (generated) images. However, a slightly higher brightness of reconstructed images in the intermediate range of brightness is evident. This could, perhaps, be mitigated by tuning the Batch Size hyperparameter.

While the monopole effectively represents the total brightness, it does not provide information about the position, shape, size, or detailed brightness distribution of the fast-rotating stars. For these aspects, higher-order moments are necessary.

The first order raw moments normalized by the respective monopole moments of the images given by

$$\begin{aligned} x_c &= \frac{M_{10}}{M_{00}} = \frac{\sum_{x,y} x \cdot I(x, y)}{\sum_{x,y} I(x, y)} \\ y_c &= \frac{M_{01}}{M_{00}} = \frac{\sum_{x,y} y \cdot I(x, y)}{\sum_{x,y} I(x, y)} \end{aligned} \quad (19)$$

represent the centroids (x_c, y_c) of the pixel brightness distribution of the images. An ideally trained GAN model should produce the centroids of the target and predicted images within a small range of pixels. A larger range would imply a low fidelity in learning the brightness distribution of ground truth images. The middle and right panels of Fig. 10 compare the centroids (x_c, y_c) of 100 predicted images with their corresponding ground truths respectively. We notice that the coordinates of the centroids of ground truth images are spread across a range of 2 pixels whereas the those of the predicted images are spread across a span of 4 pixels along x -axis and 7 pixels along y -axis. This clustering of centroids within a small scale range across all results indicates that the reconstructed images never have large offsets.

Furthermore, these calculated centroids are instrumental in analyzing the shape, size, and brightness distribution of the stars using higher-order image moments. To this end, the central moment of an image is calculated according to:

$$\mu_{pq} = \frac{1}{M_{00}} \sum_x \sum_y (x - x_c)^p (y - y_c)^q I(x, y). \quad (20)$$

The sum of p and q defines the order of the central moment.

The second order central moment of the brightness distribution of the images is analogous to the moment of inertia of a mass distribution. Fig. 11 presents the comparison of second-order central moments $(\mu_{11}, \mu_{20}, \mu_{02})$, which are used to study the structure of a fast-rotating star along the line of sight (as explained in the upcoming subsection). All three plots demonstrate an approximate equality among these moments, similar to the

monopole, thereby confirming the success of applying the Model to reconstruct images with II. The small scatter in the moments of the predicted images indicates robust learning of the Model without over-fitting.

The third-order central moments $(\mu_{30}, \mu_{03}, \mu_{21}, \mu_{12})$ of the images quantify the degree and direction of asymmetry of the brightness distribution around their respective centroids. Fig. 12 presents a comparison of all third-order moments for both the ground truth and the reconstructed image. All the four panels show a low skewness in the brightness distribution of the ground truth images. The skewness of the predicted images along the y -axis is dominated by one outlier as seen in the values of μ_{03} and μ_{12} . However, the approximately uniform distribution of skewness of the predicted images along the x -axis, with a few outliers though, as seen in the values of μ_{30} and μ_{21} suggests that this feature in the ground truth images has been picked up fairly well during the training of the Model.

6.3. The reconstructed Parameters for object

The centroids (x_c, y_c) indicate only the center of the star and its spatial location in the image. In contrast, the second-order central moments determine the orientation, semi-major axis, and eccentricity relative to the source's center (Teague 1980). These moment-based parameters fully describe the two-dimensional ellipse that fits the image data.

The orientation of a fast-rotating star along the line of sight is defined in terms of second-order central moments as

$$\theta = \frac{1}{2} \arctan \left(\frac{2\mu_{11}}{\mu_{20} - \mu_{02}} \right). \quad (21)$$

The semi-major and semi-minor axes of the stellar object are computed using the second-order central moments and are denoted as a and b , respectively.

$$\begin{aligned} a &= 2\sqrt{mp + \delta} \\ b &= 2\sqrt{mp - \delta} \end{aligned} \quad (22)$$

where,

$$mp = \frac{\mu_{20} + \mu_{02}}{2} \quad (23)$$

and

$$\delta = \frac{\sqrt{4\mu_{11}^2 + (\mu_{20} - \mu_{02})^2}}{2}. \quad (24)$$

Using the calculated axis values, the eccentricity of the fast-rotating star is determined as:

$$e = \sqrt{1 - a/b}. \quad (25)$$

Eqs. 21-25 describe the elliptical nature of the stellar object (in this case, a fast-rotating star) and provide information on its shape and size, depending on the computed values. In contrast, the brightness distribution

is characterized by skewness, which is quantified using third and higher-order moments.

7. CONCLUSION

Intensity Interferometry (II) is re-emerging as a promising technique to overcome the challenges of very long baseline interferometry in the optical wavelength range. However, compared to radio-interferometry, optical interferometry faces a major hurdle: photon correlation captures only the magnitude of the interferometric signal, resulting in a loss of phase information.

This work addresses the challenge of phase retrieval in II using a machine-learning technique, specifically a conditional Generative Adversarial Network (cGAN). Our study demonstrates that the size, shape and brightness distribution of fast rotating stars can be recovered by a Pix2Pix cGAN model trained on the combined input of the sky-image of known sources along with their respective II data. In this training the sky-image acts as the real “ground truth” and the II data acts as the “condition”. The Discriminator of our Model is trained to efficiently distinguish between the real images and fake (generated) images based on the “ground truth” images and the respective II data as the condition. The Generator is trained to generate progressively realistic images which are also consistent with the condition of the II data. The evaluation of the trained Model is then carried out by comparison of image moments of ground truth images and generated images. Specifically, the monopole, second, and third-order moments are compared. The results support the effectiveness of cGAN in achieving the stated objective.

While the results of this study highlight the significant potential of machine learning, and in particular the applicability of cGAN, for image reconstruction in II, several aspects require further refinement. First, an important factor in the reconstruction process is the extent of

Fourier plane coverage, which depends on the number of available telescopes and the total observing time. The reasonable success of this piece of work suggests that a network of higher number of telescopes providing higher number of baselines and greater coverage of the (u, v) plane signal, would play a critical role in projects of image reconstruction of more complicated stellar systems can be undertaken. Future work might explore different observatory layouts to assess their impact on image reconstruction quality. Second, detector efficiencies, which impact the signal-to-noise ratio (SNR) of actual observational data, have not yet been incorporated; addressing these factors will be crucial for more accurate SNR estimation. Third, exploring and comparing alternative methods for image generation could reveal approaches that outperform cGAN in reconstructing stellar images with II. Fourth, experimenting with different loss functions could provide additional insights into the reconstruction quality. Although further testing is needed to refine the GAN and enhance its robustness and reliability, our findings suggest that machine learning is a promising approach for phase reconstruction in II.

NOTE ON SOFTWARE

The code used for this work is available on the DOI: [10.5281/zenodo.17598807](https://doi.org/10.5281/zenodo.17598807)

ACKNOWLEDGEMENTS

Acknowledgment: One of the authors (SS) gratefully acknowledges the computing facilities and the local hospitality extended to him by the Inter-University Centre for Astronomy and Astrophysics (IUCAA), Pune, India under its Visiting Associate Programme during the preparation and finalization of this manuscript.

REFERENCES

- 1071 Abadi et al., M. 2016, arXiv preprint arXiv:1603.04467
- 1072 Abe et al., S. 2024, MNRAS, 529, 4387
- 1073 Acciari et al., V. A. 2020, MNRAS, 491, 1540
- 1074 Acharyya et al., A. 2024, The Astrophysical Journal, 966, 28
- 1076 Aleksić et al., J. 2016, Astroparticle Physics, 72, 76
- 1077 Archer, A., Aufdenberg, J. P., Bangale, P., et al. 2025, arXiv e-prints, arXiv:2506.15027
- 1079 Baumgartner et al., S. 2020, MNRAS, 498, 4577
- 1080 Coccolini et al., D. 2021, arXiv preprint arXiv:2122.11578
- 1081 Domiciano de Souza, A., Kervella, P., Jankov, S., et al. 2003, Astronomy and Astrophysics, 407, L47
- 1083 Domiciano de Souza, A., Kervella, P., Jankov, S., et al. 2005, Astronomy and Astrophysics, 442, 567
- 1085 Drawins et al., D. 2013, Astroparticle Physics, 43, 331
- 1086 Fienup, J. 1982, Applied Optics, 21, 2758
- 1087 Gamo, H. 1963, Journal of Applied Physics, 34, 875
- 1088 Gerchberg, R. W. 1972, Optik, 35, 237
- 1089 Glauber, R. J. 1963, Physical Review, 130, 2529
- 1090 Goldberger et al., M. L. 1963, Physical Review, 132, 2764
- 1091 Goodfellow et al., I. 2014, Advances in neural information processing systems, 27
- 1093 Hanbury Brown, R. & Twiss, R. Q. 1956, Nature, 177, 27

- 1094 Hanbury Brown et al., R. 1957, Proceedings of the Royal
 1095 Society of London. Series A. Mathematical and Physical
 1096 Sciences, 242, 300
- 1097 Hanbury Brown et al., R. 1958, Proceedings of the Royal
 1098 Society of London. Series A. Mathematical and Physical
 1099 Sciences, 243, 291
- 1100 Hanbury Brown et al., R. 1974, Monthly Notices of the
 1101 Royal Astronomical Society, 167, 121
- 1102 Haubois et al., X. 2009, Astronomy & Astrophysics, 508,
 1103 923
- 1104 Holmes et al., R. 2010, in Adaptive Coded Aperture
 1105 Imaging, Non-Imaging, and Unconventional Imaging
 1106 Sensor Systems II, Vol. 7818, SPIE, 175–185
- 1107 Hu, M.-K. 1962, IRE transactions on information theory, 8,
 1108 179
- 1109 Hunter, J. D. 2007, Computing in Science & Engineering, 9,
 1110 90
- 1111 Isola et al., P. 2017, in Proceedings of the IEEE conference
 1112 on computer vision and pattern recognition, 1125–1134
- 1113 Kirisits et al., C. 2024, arXiv preprint arXiv:2406.14143v2
- 1114 Le Bohec, S.; Holder, J. 2006, The Astrophysical Journal,
 1115 649, 399
- 1116 Li et al., X. 2014, in Imaging Spectroscopy, Telescopes and
 1117 Large Optics, Vol. 9298, SPIE, 92981G1–G7
- 1118 Liu, L.-C., Wu, C., Li, W., et al. 2024, arXiv preprint,
 1119 arXiv:2404.15685
- 1120 Liu et al., L.-C. 2025, Physical Review Letters, 134, 180201
- 1121 Lucy, L. B. 1967, Zeitschrift für Astrophysik, Vol. 65, p. 89,
 1122 65, 89
- 1123 Maeder, A. 1999, Astronomy & Astrophysics, 347, 185
- 1124 Martinez, A. O., Baron, F., Monnier, J. D., Roettenbacher,
 1125 R. M., & Parks, J. R. 2021, The Astrophysical Journal,
 1126 916, 60
- 1127 McAlister et al., H. A. 2005, The Astrophysical Journal,
 1128 628, 439
- 1129 Mirza et al., M. 2014, arXiv preprint arXiv:1411.1784
- 1130 Monnier, J. D., Zhao, M., Pedretti, E., et al. 2007, Science,
 1131 317, 342
- 1132 Murphy, K. P. 2022, Probabilistic machine learning: an
 1133 introduction (MIT press)
- 1134 Mustafa et al., M. 2019, Computational Astrophysics and
 1135 Cosmology, 6, 1
- 1136 Norris et al., R. P. 2021, The Astrophysical Journal, 919,
 1137 124
- 1138 Nuñez et al., P. D. 2010, in Optical and Infrared
 1139 Interferometry II, Vol. 7734, SPIE, 458–467
- 1140 Nuñez et al., P. D. 2012a, Monthly Notices of the Royal
 1141 Astronomical Society, 419, 172
- 1142 Nuñez et al., P. D. 2012b, Monthly Notices of the Royal
 1143 Astronomical Society, 424, 1006
- 1144 Pedretti, E., Monnier, J. D., ten Brummelaar, T., &
 1145 Thureau, N. D. 2009, New Astronomy Reviews, 53, 353
- 1146 Prince, S. J. 2023, Understanding deep learning (MIT
 1147 press)
- 1148 Rai, K. N., Basak, S., Sarangi, S., & Saha, P. 2025,
 1149 Resonance, 30, 45
- 1150 Rai et al., K. N. 2021, Monthly Notices of the Royal
 1151 Astronomical Society, 507, 2813
- 1152 Rai et al., K. N. 2022, Monthly Notices of the Royal
 1153 Astronomical Society, 516, 2864
- 1154 Ronneberger et al., O. 2015, in Medical image computing
 1155 and computer-assisted intervention—MICCAI 2015: 18th
 1156 international conference, Munich, Germany, October 5–9,
 1157 2015, proceedings, part III 18, Springer, 234–241
- 1158 Sato et al., T. 1978, Applied optics, 17, 2047
- 1159 Sato et al., T. 1979, Applied Optics, 18, 485
- 1160 Sato et al., T. 1981, Applied Optics, 20, 2055
- 1161 Schawinski et al., K. 2017, MNRAS, 467, L110
- 1162 Teague, M. R. 1980, Josa, 70, 920
- 1163 Teague, M. R. 1983, Journal of Opticala Society of
 1164 America, 73, 1434
- 1165 van Belle, G. T., Ciardi, D. R., Thompson, R. R., Akeson,
 1166 R. L., & Lada, E. A. 2001, The Astrophysical Journal,
 1167 559, 1155
- 1168 Virtanen et al., P. 2020, Nature methods, 17, 261
- 1169 Vogel et al., N. 2025, MNRAS, 537, 2334
- 1170 Von Zeipel, H. 1924, Monthly Notices of the Royal
 1171 Astronomical Society, Vol. 84, p. 665–683, 84, 665
- 1172 Zhang et al., J. 2020, Opt. Lett., 45, 3649
- 1173 Zhao, M., Monnier, J. D., Pedretti, E., et al. 2009, The
 1174 Astrophysical Journal, 701, 209